

1 **Seafloor observations eliminate a landslide as the source of the 1918 Puerto Rico tsunami**

2

3 U.S. ten Brink, J.D. Chaytor, C.H. Flores, Y. Wei, S. Detmer, L.C. Lucas, B.D. Andrews, and A.

4

Georgiopolou

5 Key points

6 -Seafloor observations indicate that a landslide could not be the source of the 1918 Puerto Rico

7 tsunami

8 -Tsunami from a M7.2 rupture of a two-segment fault in eastern Mona Rift fits the observations

9 well

10 -Our analysis shows the need for seafloor observations and sampling in natural hazard studies

11

12 Declaration of Competing interests: The authors acknowledge there are no conflicts of interest
 13 recorded

14

15 **Abstract**

16 The October 11, 1918, devastating tsunami in northwest Puerto Rico, had been used as an

17 example for earthquake-induced landslide tsunami hazard. Three pieces of evidence pointed to a

18 landslide as the origin of the tsunami: the discovery of a large submarine landslide scar from

19 bathymetry data collected by shipboard high-resolution multibeam sonar, reported breaks of

20 submarine cable within the scar, and the fit of tsunami models to flooding observations. Newly

21 processed seafloor imagery collected by remotely-operated-vehicle (ROV) show, however,

22 pervasive Fe-Mn crust (patina) on the landslide walls and floor, indicating that the landslide scar

23 is at least several hundred years old. ¹⁴C dates of sediment covering the landslide floor verify this

24 interpretation. Although we have not searched the region systematically for an alternative

25 tsunami source, we propose a possible source, a two-segment normal fault rupture along the
26 eastern wall of Mona Rift. The proposed fault location matches published normal faults with
27 steep bathymetry and is close to the ISC-GEM catalog locations of the 1918 main shock and
28 aftershocks. ROV observations further show fresh vertical slickensides and rock exposure along
29 the proposed fault trace. Hydrodynamic models from a M7.2 earthquake rupture along the
30 eastern wall of the rift faithfully reproduce the reported tsunami amplitudes, polarities, and
31 arrival times. Our analysis emphasizes the value of close-up observations and physical samples
32 to augment remote sensing data in natural hazard studies.

33

34 **1. Introduction**

35 The damaging October 11, 1918 earthquake offshore NW Puerto Rico was followed within
36 minutes by a tsunami that mostly affected the west coast of Puerto Rico. The tsunami caused
37 more than 100 casualties and the damage exceeded \$4,000,000 in 1918 U.S. dollars (Reid and
38 Taber, 1919). A repeat of such an event today has the potential to be catastrophic due to the
39 increased population, tourism, and development along the coast of Puerto Rico. Hence, the
40 interest in understanding the source of the event. The location and focal mechanism of the
41 earthquake and aftershocks could not be determined with certainty, given the small number of
42 operating seismometers globally and the lack of any local instruments at the time (Location
43 quality of B and C in the International Seismological Center-Global Earthquake Model (ISC-
44 GEMS) catalog (Di Giacomo et al., 2018). The most recent estimate by ISC-GEMS, also adopted
45 by the USGS Advanced National Seismic Systems (ANSS) Comprehensive Catalog (ComCat),
46 is several kilometers east of the eastern boundary of Mona Rift (Figure 1) ($18^{\circ}42'$ $-67^{\circ}11.34'$)
47 with some aftershocks of estimated magnitudes between M5.8 and 6.35, were located along the

48 eastern boundary of the rift (ISC-GEMS catalog). An earlier epicentral estimate (Russo and
49 Bareford, 1993), quoted by Doser et al. (2005), was located within Mona Passage ($18^{\circ}16.8'$ -
50 $67^{\circ}37.2'$, Figure 1) with an estimated location uncertainty of 50 km. Note, however, seismic and
51 multibeam bathymetry data do not show a recent seafloor or sub-seafloor rupture in the vicinity
52 of the Doser et al. (2005) epicenter (Chaytor and ten Brink, 2010). The proposed magnitude of
53 the main shock is $M_w7.1\pm0.3$ (Di Giacomo et al., 2018) to $M_w7.2$ (Doser et al., 2005), and the
54 proposed focal depth is 15 km (ISC-GEMS catalog). The proposed focal mechanism is normal
55 slip on a steep N-S fault, but with large uncertainties; namely, strike, dip, and rake of $207^{\circ} \pm 22$,
56 $54^{\circ} \pm 8$, and $-127^{\circ} \pm 28$, respectively (Doser et al., 2005).

57

58 Reid and Taber visited the area shortly after the earthquake and tsunami and took detailed notes
59 of the events based on interviews with eyewitnesses and inspections of the damage. Their
60 meticulous notes and insightful interpretations, published in the Bulletin of the Seismological
61 Society of America in 1919, formed the basis of later modeling of the tsunami source and are
62 summarized in Table 1. Reid and Taber (1919) observed that the wave amplitude was highest
63 along the northwest corner of the island and decreased to the south and west. The wave was
64 reported to have come from the NW. The water along the shoreline first receded exposing reefs
65 never exposed at low tide before returning quickly. They determined the maximum wave height
66 from visible damage and from eyewitness testimonies and interviewed eyewitnesses about the
67 estimated time between the beginning of felt shaking and the initial withdrawal of the sea. The
68 initial felt shaking was vertical, which they contrasted with the initial horizontal felt shaking
69 during the San Francisco 1906 earthquake. Mercado and McCann (1998) modeled Reid and
70 Taber's (1919) tsunami observations by assuming rupture along a fault trace marked by a dashed

71 blue line in Figure 1. Their fault trace has a total length of 67 km and runs along the base of the
72 entire east wall of Mona Rift and crosses the rift diagonally to the SW toward Desecheo Island at
73 its southern end. Mercado and McCann (1998) assumed an average downdip width of 23 km and
74 a slip of 4 m resulting in an earthquake magnitude of 7.47. Their model results, however, did not
75 fit some of the documented observations. An initial positive polarity (i.e., flooding) of 0.7 m and
76 0.4 m was predicted in Aguadilla and Mayagüez, respectively, contrary to eyewitness reports.
77 The maximum amplitudes were also much lower than observed. Some of the discrepancy
78 between model predictions and the observations could probably be attributed to the coarser
79 bathymetry grid available at the time (9.25 km cell size, interpolated near shore to a 90 m cell
80 size), to the lower resolution numerical model that was utilized, and also to the choice of fault
81 trace location and orientation.

82
83 The discrepancy between the tsunami observations and Mercado and McCann's (1998)
84 predictions from a fault rupture model led López-Venegas et al. (2008) to explore an alternative
85 tsunami source. High-resolution multibeam bathymetry and seismic reflection data collected
86 since Mercado and McCann's publication revealed a 9 km x 9 km x 0.14 km landslide scar at the
87 southern end of Mona Rift (Figure 1 inset A) with an estimated volume of evacuated material of
88 10 km³ (López-Venegas et al., 2008). Breaks and damage to submarine telegraph cables assumed
89 to be due to burial under and impact by sedimentary debris were reported within the scar area
90 following the earthquake (Reid and Taber, 1919). The cable breaks and damage were located
91 within the mapped landslide scar. This led López-Venegas et al. (2008) to propose that the
92 tsunami was caused by an earthquake-triggered slope failure, which produced the scar (Figures 1
93 and 2). A similar event of earthquake-triggered landslide and turbidity currents generating a

94 deadly tsunami was documented in Canada's Grand Banks in 1929 (Fine et al., 2005, and
95 references therein). The López-Venegas et al. (2008) landslide hydrodynamic model produced
96 the initial negative polarity of the wave reaching shore, but the calculated wave amplitude was
97 generally too high. Hornbach et al. (2008) reduced the volume of the modeled landslide and
98 modified its shape to fit the observed wave amplitude. A more sophisticated modeling scheme of
99 landslide-generated tsunami by López-Venegas et al. (2015) simulated the tsunami amplitude at
100 three of the reported sites (Pt. Borinquen, Aguadilla, and Pt. Higüero; see [Figure 1](#) for location),
101 but their calculated amplitudes (4.8-5.4 m, 4.8-7.2 m, and 7.1 m, respectively) did not match the
102 Reid and Taber (1919) observed values (4.5 m, 2.4-3.4 m, and 5.2 m, respectively).

103

104 In this paper, we revisit the landslide-generated tsunami hypothesis proposed by López-Venegas
105 et al. (2008) using video of the seafloor in the floor and walls of the landslide scar, collected by a
106 remotely operated vehicle (ROV) and processed into a Structure-from-Motion (SfM) 3-D
107 photogrammetric model. We also date core samples to determine the scar's age. We find that the
108 landslide scar is older than 1918 and was likely not formed by that earthquake. We propose
109 instead an earthquake rupture source fault which fits the negative polarity, amplitude, and arrival
110 time of the tsunami in the reported tsunami sites, and we present seafloor images of possible
111 fault plane striations along the proposed source fault.

112

113 **2. Data**

114 **2.1 Seafloor imagery and photogrammetry**

115 Seafloor imagery and sediment core samples within the landslide scar and along its walls were
116 collected by the ROV *Hercules* during Dive H1301 of the Ocean Exploration Trust expedition

117 NA-035 aboard the ship E/V *Nautilus* from October 4–18, 2013 (ten Brink et al., 2014). The
118 ROV *Hercules* tethered to the E/V *Nautilus*, is equipped with a high-definition video camera, a
119 manipulating arm for collecting rock and biological samples, push cores for collecting sediment
120 samples, and equipment for sampling water. Throughout the dives *Hercules* was illuminated by
121 its companion ROV *Argus* hovering above it. Additional seafloor imagery of the proposed fault
122 wall was collected during Dive 05 of the NOAA’s Ocean Exploration Program expedition
123 EX1502 from April 9-30, 2015 aboard the NOAA Ship Okeanos Explorer using its tethered
124 ROV *Deep Discoverer* (Kennedy et al., 2015). Throughout the dives, *Deep Discoverer* was
125 illuminated by its companion ROV *Seirios* hovering above it.

126

127 The high-definition video collected by both *Hercules* and *Deep Discoverer* was processed into a
128 3-D photogrammetric model. First, individual frames were extracted from the dive videos at one
129 second increments using Agisoft Metashape Pro©. Because video images at water depths of
130 1000-4000 m are only illuminated by the ROV light, their color, contrast, and brightness vary
131 between and within each frame due to the varying illumination distance and the effect of
132 differential light attenuation by sea water. To compensate for the varying illumination distances,
133 we balanced the brightness and contrast of the frames using OpenCV’s Contrast Limited
134 Adaptive Histogram Equalization (CLAHE) algorithm in Python. The balanced images were
135 then imported into Agisoft Metashape Pro© for processing, where some color balance and
136 additional brightness modification was carried out manually in addition to masking out the edges
137 of the ROV and deleting frames where the ROV was not moving. Although image intensity was
138 balanced, the image color depends on the light source distance from the target rock, resulting in
139 yellower surfaces closer to the light source and bluer surfaces farther away. From here, common

140 processing steps were followed (e.g., Hansman and Ring, 2019) to attain a 3-D photogrammetric
141 model. The steps included aligning the images to acquire a sparse elevation/depth point cloud,
142 refining and optimizing the camera paths using known distances and control points, building a
143 dense point cloud from the imagery, building a 3-D mesh from the dense cloud, adding
144 navigation for georeferencing, and finally draping the imagery onto this 3-D mesh, and stitching
145 3D models into a larger matrix. These processing steps were carried out using Agisoft Metashape
146 Pro©. 3-D manipulation and display of the virtual outcrops were carried out using VOG Lime©.

147

148 **2.2 Hydrodynamic modeling**

149 Tsunami simulations were carried out using the Method of Splitting Tsunamis (MOST) based on
150 the depth-integrated nonlinear shallow water equations (Titov et al., 2016). MOST simulation
151 starts from tsunami source generation by instantaneous co-seismic deformation of the seafloor.
152 MOST then efficiently computes tsunami propagation and inundation using three nested grids to
153 achieve increasing resolution of nearshore bathymetry and topography. Because it is the standard
154 model used operationally at the National Oceanic and Atmospheric Administration (NOAA)'s
155 Tsunami Warning Centers, the MOST model has been extensively verified and validated using
156 laboratory experiments, model benchmarks, and modern tsunami events (Synolakis et al., 2008;
157 Tang et al., 2012; 2016; Wei et al., 2008; 2013). Nearshore grids of 1/3 arc sec (~10 m)
158 resolution were created using newer bathy/topo lidar (NOAA Center of Environmental
159 Information, NCEI) collected since Andrews et al. (2013) database for the NE Caribbean was
160 published. Tsunami runup and inundation are computed. Elsewhere a reflective boundary, and
161 thus no inundation calculation, is applied along the 1-m depth contour offshore at a grid

162 resolution of 3 arc sec (~ 90 m). The MOST model uses a uniform bottom friction (Manning's)
163 coefficient of 0.03 in all telescoped grids.

164

165 **3. Observations – Landslide scar is older than the 1918 earthquake**

166 **3.1 Seafloor imagery**

167 Seismic reflection data show that the landslide scar is cut into a layered carbonate platform that
168 had been tilted downward to the north, and both the walls and floor are made of competent
169 limestone and dolomite (López-Venegas et al., 2008). Our seafloor imagery observations show
170 that the floor of the scar is heavily sedimented but shows evidence of jagged texture oriented in a
171 downhill direction (e.g., Figure 3) possibly representing frictional damage from the movements
172 of cohesive rock against a cohesive bottom at the time of failure. The gouges are 4-8 m wide, and
173 their edges range from a few centimeters to 1.5 meters tall. The massive or layered rock faces,
174 exposed along the edges of some gouges, are covered with black patina, and show no sign of
175 fresh breaks (e.g., Figure 3).

176

177 The observed black patina is a Fe-Mn crust composed of Mn oxides and Fe oxyhydroxides with
178 Mn/ Fe ratios mostly around 1–2, which precipitate from seawater and envelope exposed rocks
179 ((Koschinsky and Hein, 2017; Figure 4A, B). The patina is found throughout the world oceans.
180 Except near hydrothermal vents, Fe-Mn crust grows at a very slow rate (1-5 mm/Ma, Maciag et
181 al., 2019; 3.05-4.85 mm/Ma at the water depths of the dive, 1250-2000 m, Conrad et al., 2017).
182 A grab sample taken by ROV *Hercules* (Figure 4C) along a deep gulley in the scar floor (See
183 Figure 5A for location) shows a thin (>1 mm) veneer of Fe-Mn crust on limestone. (Figure 4B).
184 Even a 1-micron-thick crust requires 200-1000 years to develop. Hence, the observation of Fe-

185 Mn crust on the gouges suggests that the gouges did not form by an earthquake-triggered
186 landslide in 1918.

187

188 The ROV traversed a narrow gully cut into the scar's floor (Figure 5A). The gully's wall is
189 layered and most of the rock face is black indicating the presence of Fe-Mn crust. A few rocks at
190 the top bench of the wall appear to lack patina. The shaking from the 1918 earthquake could
191 have dislodged a few rocks which rolled downslope. However, the gully itself does not seem to
192 have been carved by a landslide during the 1918 earthquake. Another gully shows a white rock
193 face at the bottom few meters of its wall (Figure 5B). The remainder of the gully wall, however,
194 is composed of rock ledges covered by black patina and by talus, suggesting that they were not
195 affected by the shaking from the 1918 earthquake. Hence, it appears that some rocks may have
196 been dislodged sporadically from a pre-existing floor of the landslide scar.

197

198 The ROV traversed the eastern and southern scar walls, each >100 m high (See Figure 6A, B for
199 sections of these walls). The southern wall is layered showing steep competent rock faces
200 separated by talus and rubble (Figure 6A). Signs of downslope sediment flow are visible, but
201 none of them appear to be mass transport deposits from a high-volume landslide. All the exposed
202 rock faces are black, presumably because they are covered by Fe-Mn crust (Figure 6A). The
203 eastern wall appears to be composed of a continuous rocky slope with pitted texture and potential
204 layering at the base of the scarp (Figure 6B). The primary rock texture may be hidden by the
205 texture of the Fe-Mn crust. Fresh rock surfaces were not observed along either the eastern or
206 southern scar walls, suggesting that the scar's walls were created before 1918. In summary,
207 neither the floor nor the walls of the scar indicate that they formed recently, hence, we propose

208 that the previously modeled landslide scar predates the 1918 earthquake and could not be the
209 source of the observed tsunami.

210

211 **3.2 Sediment cores**

212 Surficial sediments recovered from ROV push cores collected within the scar (PC-038, see
213 Figure 2 for location and Figure 4D for image of the push core being pulled out of the sediment)
214 and immediately adjacent to the crest of the eastern headwall (PC- 040, Figure 2) are similar in
215 both texture and composition. Push cores 038 and 040 penetrated 14 cm and 18 cm, respectively,
216 but did not reach the hard rock floor of the landslide scar. Sediment recovery was close to 100%.
217 The sediments are composed of mixed intact and fragmented biogenic carbonate material
218 dominated by foraminifera and pteropod tests with a small fraction of gastropod and other
219 mollusk shells. The minor non-carbonate fraction of the sediment is composed of siliceous
220 spicules and detrital lithic fragments and mineral grains. The sediments are quite uniform down
221 the cores and show no obvious signs of transport by a landslide. Texturally, the bulk of the
222 sediments are classified as very poorly sorted (sorting > 2) clayey silts (mean grain size between
223 8 and 6.55 ϕ), with minor variations in the major grain size fractions down the length of the short
224 cores. Calcium carbonate content of the $> 63 \mu\text{m}$ fraction of these sediments determined by loss
225 on ignition (Chaytor et al., 2021), exceeds 60 % (by weight).

226

227 Accelerator mass spectrometry (AMS) ^{14}C dating was performed on planktonic foraminifera
228 extracted from a single 1 cm thick interval in ROV push core 038, located 3 cm below the
229 seafloor within the scar floor at a water depth of 1973 m (See Figure 2 for location). A calibrated
230 age of 440 ± 120 years BP was determined. The calibrated age (BP) was calculated using Calib

231 8.2 (Stuiver et al., 2021) and the Marine20 calibration curve (Heaton et al., 2020), with only the
232 550-year reservoir correction (i.e., no delta-R) applied. Based on this age, sedimentation rate
233 appears to be relatively high on the scar's floor (between 6.8 cm/1000 yr). We conclude that
234 sediment accumulation above the floor of the landslide scar likely took hundreds if not a few
235 thousand years to develop.

236

237 **4. Discussion – Segmented fault as tsunami source**

238 The landslide scar in southern Mona Rift likely formed several hundreds to thousands of years
239 before 1918, hence, the tsunami could not have been generated by the associated landslide
240 movement, as previously suggested in López-Venegas et al. (2008, 2015) and Hornbach et al.
241 (2008). Fe-Mn crust covering both the side escarpment and gouges and a gully on the scar's
242 floor attest to an age of at least a few thousand years because of the slow rate of mineral
243 precipitation from seawater onto the rock surface. A thick sediment cover of the scar's floor is
244 dated at being older than 1918 and another obvious landslide source was not identified.

245 Consequently, we re-evaluate the possibility of a fault rupture as the source of the tsunami.

246 **4.1 Tsunami models**

247 We did not explore systematically an alternative tsunami source, but we propose here one
248 possible source based on bathymetry, seismic profiles, dive observations, and the description of
249 the earthquake. Our proposed fault trace is 40 km long and follows the steepest part of the
250 bathymetric slope along the eastern and SE walls of Mona Rift (Figure 1). Seismic reflection
251 profiles (Figure 7, and Figure 8 in Mondziel et al., 2010; See Figure 1 for locations) suggest a
252 possibly active normal fault across both orientations (Figure 1). Dive observations discussed
253 below show a rock face with slickensides across the N-S segment. Reid and Taber (1919)

254 described a severe shaking event followed ~two minutes later by a less severe one. We propose a
255 two-segment fault rupture scenario: a rupture of 29-km-long N-S-oriented fault followed by a
256 rupture of an 11-km-long NW-SE-oriented fault (red rectangles in Figure 1; Table 2). The
257 centers of the two faults segments are ~20 km, which for an average water depth of ~3000 m will
258 lead to positive interference between tsunami waves generated by two ruptures two minutes
259 apart. The earthquake was initially felt as vertical motion, indicating normal faulting, which Reid
260 and Taber (1919) contrasted with their experience during the 1906 San Francisco earthquake.

261
262 The earthquake magnitude was assumed to be Mw7.2 following Doser et al. (2005). A downdip
263 width of $W=15$ km was assumed starting 1 km below the seafloor, to avoid a singularity in the
264 calculation (Figure 8). A generic dip of 60° was modeled following Doser et al. (2005) focal
265 plane solution, the felt motion by eyewitnesses, and the suggested normal motion from seismic
266 reflection data (Figure 7; Mondziel et al., 2010). The modeled fault parameters are listed in Table
267 2.

268
269 The calculated tsunami amplitude, polarity, and arrival time from this rupture source fit Reid and
270 Taber's (1919) reported observations (Table 1, Figure 9). The misfits in wave amplitude are < 1
271 m. Reid and Taber's (1919) observations did not specify the tidal level during the tsunami, which
272 around Puerto Rico is ≤ 0.5 m (<https://tidesandcurrents.noaa.gov/>). Reid and Taber (1919) did
273 not specify the tsunami observation location along the Aguadilla shoreline. However, LaForge
274 and McCann (2017) and López-Venegas et al. (2015) used archival petitions for funds to repair
275 tsunami damage to identify the exact street in Aguadilla, which suffered the maximum damage.
276 The shoreline coordinate facing that street was used in Table 1. A map of the maximum
277 predicted flooding from the two-segment fault rupture is shown in Figure 10.

278

279 The modeled first wave polarity at all reported sites fits the eyewitness reports. Reid and Taber
280 (1919) reported initial withdrawal in all locations except in Loíza (Figure 9). Except for
281 Boquerón, the calculated arrival time fit the eyewitness reports in Reid and Taber (1919).
282 Flooding at 5-6 minutes and 25-30 minutes after the shaking was felt was reported in Aguadilla
283 and Mayagüez, respectively. A withdrawal followed by flooding 25-30 minutes after the
284 earthquake was reported in Loíza, and withdrawal about 1 hour after the earthquake was reported
285 in Boquerón.

286

287 **4.2. Fault plane imagery**

288 Exposed fault planes may have been encountered on a dive across the fault trace proposed by our
289 tsunami model. Video observations collected by ROV *Deep Discoverer* along the east wall of
290 Mona Rift between depths of 3300-4000 m, encountered Late Cretaceous to Middle Eocene
291 meta-volcanic and plutonic rocks that form the core of Puerto Rico Island underlying the Late
292 Oligocene to Pliocene platform carbonate sequence. Slickensides (smooth striated and
293 corrugated surface) were identified at depths of 3884-3882 m (Figures 1A, 11A). Slickensides
294 are thought to be produced by frictional rock movement along a fault. Note that the rock surface
295 of the slickensides is free of Fe-Mn crust, indicating that this rock face is likely recently exposed.
296 The striations point downward indicating sub-vertical movement. Their slope, $20\pm 8^\circ$, is lower
297 than the 60° slope assumed in our tsunami model, and their dip direction is $190^\circ\pm 10^\circ$, suggesting
298 that the striations have developed along a subsidiary fault plane. A smooth rock face lacking
299 patina is also observed a few meters above the striations (Figures 1A, 11B). A blueish-color
300 exposure at the bottom of the image with possible striations may be a small fault plane exposure

301 and/or a freshly exposed blueschist (Enlargement in Figure 11B). The dip direction of this
302 exposure is 280° . A late Cretaceous blueschist belt extending along the continental slope
303 eastward from Samaná Peninsula in the NE Dominican Republic was proposed by Perfit et al.
304 (1980) from analysis of outcrops and dredges.

305

306 **5. Conclusions**

307 The source of the devastating 1918 western Puerto Rico tsunami had previously been ascribed to
308 both an earthquake fault rupture (Mercado and McCann, 1998) and an earthquake-triggered
309 landslide (López-Venegas et al., 2008; 2015; Hornbach et al., 2008). Documented landslide
310 tsunami sources are rare, and the landslide source for the 1918 tsunami had been cited as an
311 example for landslide tsunami hazards (e.g., National Research Council, 2011). The landslide
312 source suggestion was based on the then-newly available ship-board high-resolution multibeam
313 bathymetry and seismic reflection data, coupled with reports about submarine cable breaks
314 within the landslide scar area (Reid and Taber, 1919). An in-situ examination of the floor and
315 walls of the landslide scar, using high-definition video from a remotely operated vehicle (ROV),
316 and core samples collected by the ROV suggest, however, that the scar is at least several hundred
317 years old and therefore the landslide that formed could not have been triggered by the 1918
318 earthquake. The evidence includes a relatively thick sediment cover of the hard carbonate scar
319 floor, dated at several hundred years old or more, and the observations of extensive Fe-Mn crust
320 of the exposed rock faces of the eastern and southern escarpment, the gouges in the scar floor,
321 and in gullies cut into the scar floor. Published estimates of Fe-Mn crust precipitation from
322 seawater in the absence of hydrothermal activity is 1-5 mm/Ma. The reported submarine cable

323 damage and breaks could be caused by smaller rock falls from steep outcrops, and not by the
324 presumed movement of a 140 m thick, 9 km wide tsunami-generating landslide.

325
326 We propose an alternative tsunami source, namely, a two-segmented normal fault rupture along
327 the steepest parts of the eastern wall of Mona Rift NW of Puerto Rico. Our proposed fault
328 rupture has a total magnitude of $M_w 7.2$ and parameters that are compatible with seismic
329 reflection observations and with seismic analysis of the historical seismograms (Di Giacomo et
330 al., 2018; Doser et al., 2005). Although we have not performed a rigorous search for the best
331 tsunami source location and parameters, our hydrodynamic model simulates with fidelity the
332 amplitudes, the first wave polarities, and the arrival times at eight sites along western and
333 northern Puerto Rico, which were reported by Reid and Taber (1919). An ROV dive along the
334 proposed ruptured fault reveals possible corrugated striations in the exposed hard rock
335 (slickensides) that can be interpreted as being formed by friction along a fault plane. Some of the
336 hard rock face in the surrounding area is devoid of Fe-Mn crust. Our analysis, thus, demonstrates
337 the importance of in-situ observations and sampling for natural hazard studies in the ocean.

338

339 **Data and resources**

340 Videos collected during NOAA's Ocean Exploration cruise EX1502 are available from NOAA's
341 video archive portal <https://www.ncei.noaa.gov/access/ocean-exploration/video/>. Core samples
342 are available at: <https://web.uri.edu/gso/research/marine-geological-samples-laboratory/>. Ocean
343 Exploration Trust videos from expedition NA-035 are available upon request at
344 <https://nautiluslive.org/science/data-management>. Seismic parameters of the 1918 earthquake
345 were retrieved from the ISC-GEMS catalog at <http://doi.org/10.31905/D808B825> accessed

346 6/6/2022. OpenCV's (<https://opencv.org>) Contrast Limited Adaptive Histogram Equalization
347 (CLAHE) algorithm can be downloaded from the openCV package <https://opencv.org/releases/>
348 The seismic profile in Figure 7 is available from [https://walrus.wr.usgs.gov/namss/survey/p-30-](https://walrus.wr.usgs.gov/namss/survey/p-30-06-cb/)
349 [06-cb/](https://walrus.wr.usgs.gov/namss/survey/p-30-06-cb/)

350 Following is the description of the observed tsunami arrival times and their polarities in Reid and
351 Taber (1919): Agudilla: *“Estimates of the time interval between the earthquake shock and the*
352 *arrival of the sea wave, made by different observers, range from four to seven minutes, one of the*
353 *best being five to six minutes.”* Mayagüez: *“In the interval between the earthquake and the*
354 *arrival of the sea wave, an automobile traveled from the Central Corsica near Rincon to*
355 *Mayagüez, a trip that is estimated to require twenty-five or thirty minutes.”* El Boqueron: *“An*
356 *observer states that the ocean withdrew about an hour after the earthquake, the water going out*
357 *gradually during a period of twenty minutes.”* Loíza: *“..reported to have subsided and then to*
358 *have risen about one meter above normal, the phenomenon occurring twenty-five or thirty*
359 *minutes after the earthquake.”*

360

361 **Acknowledgments:**

362 We are indebted to Dr. Robert Ballard and Ocean Exploration Trust and to NOAA's Ocean
363 Exploration Program for the use of their ships, ROVs, and technical expertise. We thank Dwight
364 Coleman, Amanda Demopoulos, Nicole Reineault, Brian Kennedy, Mike Cheadle, Andrea
365 Quattrini and the rest of the onboard and remote participants in cruises NA-035 and EX1502.
366 Bill Danforth helped with the initial processing steps. Helpful reviews by Wayne Baldwin,
367 Matias Carvajal, and Alberto López-Venegas are gratefully acknowledged. Yong Wei's work is
368 funded by the Cooperative Institute for Climate, Ocean, & Ecosystem Studies (CIOCES) under

369 NOAA Cooperative Agreement NA20OAR4320271, Contribution No. 2022-1234, PMEL
370 Contribution Number 5401. Simon Detmer's and Lilian Lucas's work was funded by the Woods
371 Hole Oceanographic Institution Summer Student Fellowship. Aggeliki Georgiopoulou thanks the
372 Fulbright Foundation and Geological Survey Ireland for enabling her research stay at USGS
373 Woods Hole Coastal and Marine Science Center. Any use of trade, firm, or product names is
374 for descriptive purposes only and does not imply endorsement by the U.S. Government.

375

376 **References**

- 377 Andrews, B.D., U.S. ten Brink, W.W. Danforth, J.D. Chaytor, J-L Granja-Bruna, P. Llanes
378 Estrada, and A. Carbo-Gorosobel (2013) Bathymetric terrain model of the Puerto Rico Trench
379 and Northeast Caribbean for marine geological investigations, USGS OFR 2013-1125.
- 380 Chaytor, J.D. and U.S. ten Brink (2010) Extension in mona passage, Northeast Caribbean.
381 *Tectonophysics*, 493, 74-92.
- 382 Chaytor, J.D., M.S. Ballard, B.J. Buczkowski, J.A. Goff, K.M. Lee, A.H. Reed, and A.A.
383 Boggess (2021). Measurements of geologic characteristics and geophysical properties of
384 sediments from the New England Mud Patch. *IEEE Journal of Oceanic Engineering*.
- 385 Conrad, T., J.R. Hein, A. Paytan, A. and D.A. Clague (2017) Formation of Fe-Mn crusts within a
386 continental margin environment. *Ore Geology Reviews* **87** 25-40.
- 387 Di Giacomo, D., E.R. Engdahl and D.A. Storchak (2018). The ISC-GEM Earthquake Catalogue
388 (1904–2014): status after the Extension Project, *Earth Syst. Sci. Data*, 10, 1877-1899, doi:
389 [10.5194/essd-10-1877-2018](https://doi.org/10.5194/essd-10-1877-2018).

390 Doser, D., Rodríguez, C., Flores, C., & Mann, P. (2005). Historical earthquakes of the Puerto
391 Rico-Virgin Island region. *Active tectonic and seismic hazards of Puerto Rico, the Virgin*
392 *Islands, and offshore areas*. Mann, P. (Ed.), 103-114.

393 Fine, I.V., A.B. Rabinovich, B.D. Bornhold, R.E. Thomson, and E.A. Kulikov (2005). The
394 Grand Banks landslide-generated tsunami of November 18, 1929: preliminary analysis and
395 numerical modeling. *Mar. Geol.* **215** 45-57.

396 Hansman, R.J. and Ring, U., 2019. Workflow: From photo-based 3-D reconstruction of remotely
397 piloted aircraft images to a 3-D geological model. *Geosphere*, *15*, 1393-1408.

398 Heaton, T.J., P. Köhler, M. Butzin, E. Bard, R.W. Reimer, W.E Austin, C.B. Ramsey, P.M.
399 Grootes, K.A. Hughen, B. Kromer, and P.J. Reimer (2020). Marine20—the marine
400 radiocarbon age calibration curve (0–55,000 cal BP). *Radiocarbon* **62** 779-820.

401 Hornbach, M.J., S.A. Mondziel, N.R. Grindlay, C. Frohlich, C. and P. Mann, 2008. Did a
402 submarine slide trigger the 1918 Puerto Rico tsunami?. *Sci. Tsunami Haz.*, *27*, 22-31.

403 Kennedy, B.R.C., K. Cantwell, D. Sowers, A.M. Quattrini, M.J. Cheadle, L. McKenna
404 (2015). EX1502L3 Expedition Report- Oceana Profundo 2015: Exploring Puerto Rico's
405 Seamounts, Trenches, and Troughs. Office of Ocean Exploration and Research, Office of
406 Oceanic & Atmospheric Research, NOAA, Silver Spring, MD 20910. OER Expedition Rep.
407 2015-02-03, 93 p. doi:10.7289/V5NG4NM8

408 Koschinsky, A. and Hein, J.R. (2017). Marine ferromanganese encrustations: archives of
409 changing oceans. *Elements*, *13*, 177-182.

410 LaForge, R. and W.R. McCann (2017). Address- level effects in Aguadilla, Puerto Rico, from
411 the 1918 Mw 7.3 earthquake and tsunami. *Seism. Res. Lett.* **88** 1316-1321.

412 López -Venegas, A.M., U.S. ten Brink and E.L. Geist (2008). Submarine landslide as the source
413 for the October 11, 1918 Mona Passage tsunami: Observations and modeling. *Mar. Geol.* **254**
414 35-46.

415 López-Venegas, A.M., Horrillo, J., Pampell-Manis, A., Huérfano, V. and Mercado, A. (2015).
416 Advanced tsunami numerical simulations and energy considerations by use of 3D–2D coupled
417 models: The October 11, 1918, Mona passage tsunami. *Pure Appl. Geophys.* **172** 1679-1698.

418 Maciąg, Ł., D. Zawadzki, G.A. Kozub-Budzyń, A. Piestrzyński, R.A. Kotliński, and R.J. Wróbel
419 (2019). Mineralogy of cobalt-rich ferromanganese crusts from the Perth Abyssal Plain (E
420 Indian Ocean). *Minerals*, **9** 84.

421 Mercado, A., and W.R. McCann, (1998). Numerical simulation of the 1918 Puerto Rico tsunami.
422 *Natural Hazards*, **18** 57-76.

423 Mondziel, S., N. Grindlay, P. Mann, A. Escalona and L. Abrams (2010). Morphology, structure,
424 and tectonic evolution of the Mona canyon (northern Mona passage) from multibeam
425 bathymetry, side- scan sonar, and seismic reflection profiles. *Tectonics*, **29**.

426 National Research Council (2011). Tsunami Warning and Preparedness: An Assessment
427 of the U.S. Tsunami Program and the Nation's Preparedness Efforts. Washington,
428 DC: The National Academies Press. <https://doi.org/10.17226/12628>.

429 Perfit, M.R., B.C. Heezen, M. Rawson and T.W. Donnelly (1980). Chemistry, origin and
430 tectonic significance of metamorphic rocks from the Puerto Rico Trench. *Mar. Geol.* **34** 125-
431 156.

432 Reid, H. F., & Taber, S. (1919). The Porto Rico Earthquakes of October-November, 1918. *Bull.*
433 *Seism. Soc. Am.*, **9** 95-127.

434 Russo, R.M. and Bareford, C. (1993). Historical seismicity of the Caribbean region, 1933–1963.
435 In *Caribbean Conference on Volcanism, Seismicity and Earthquake Engineering*. University
436 of the West Indies, Trinidad.

437 Stuiver, M., P.J. Reimer, and R. Reimer (2021). CALIB radiocarbon calibration 8.2. URL
438 <http://calib.org/calib/calib.html> (accessed 3.31. 21).

439 Synolakis, C. E., Bernard, E. N., Titov, V. V., Kanoglu, U., & Gonzalez, F. I. (2008). Validation
440 and verification of tsunami numerical models. *Pure Appl. Geophys.* **165** 2197-2228.

441 Tang, L., Titov, V.V., Bernard, E.N., Wei, Y., Chamberlin, C., Newman, J.C., Mofjeld, H.,
442 Arcas, D., Eble, M., Moore, C., Uslu, B., Pells, C., Spillane, M.C., Wright, L.M., and Gica, E.
443 (2012). Direct energy estimation of the 2011 Japan tsunami using deep-ocean pressure
444 measurements. *J. Geophys. Res.*, **117** C08008, doi: 10.1029/2011JC007635.

445 Tang, L., V.V. Titov, C. Moore and Y. Wei (2016). Real-time Assessment of the 16 September
446 2015 Chile Tsunami and Implications for Near-Field Forecast, *Pure Appl. Geophys.* **173** 369-
447 387, doi: 10.1007/s00024-015-1226-3.

448 ten Brink, U., Coleman, D.F., Chaytor, J., Demopoulos, A.W.J., Armstrong, R., Garcia-Moliner,
449 G., Raineault, N.A., Andrews, B., Chastain, R., Rodrigue, K. and Mercier- Gingras, M.
450 (2014). Earthquake, landslide, and tsunami hazards and benthic biology in the Greater
451 Antilles. *Oceanography*, **27** pp.34-5.

452 Titov, V.V., U. Kânoğlu, and C. Synolakis (2016). Development of MOST for real-time tsunami
453 forecasting. *J. Waterw. Port Coast. Ocean Eng.*, 142, 03116004, doi:
454 10.1061/(ASCE)WW.1943-5460.0000357.

455 Wei, Y., Bernard, E.N., Tang, L., Weiss, R., Titov, V.V., Moore, C., Spillane, M., Hopkins, M.,
456 and Kânoğlu, U. (2008). Real-time experimental forecast of the Peruvian tsunami of August
457 2007 for U.S. coastlines. *Geophys. Res. Lett.* **35** L04609, doi: 10.1029/2007GL032250.

458 Wei, Y., Chamberlin, C., Titov, V.V., Tang, L., and Bernard, E.N. (2013). Modeling of the 2011
459 Japan tsunami - Lessons for near-field forecast. *Pure Appl. Geophys.* **170**, doi:
460 10.1007/s00024-012-0519-z, 1309–1331.

461

462

463 **Mailing addresses of authors:**

464 Uri ten Brink, Jason Chaytor, Claudia Flores, and Brian Andrews – U.S. Geological Survey, 384

465 Woods Hole Rd., Woods Hole, MA 02543 USA

466 Simon Detmer – Dept. of Geology, Geography, and Environment, Calvin University, Grand

467 Rapids, MI, 49546 USA

468 Yong Wei - Cooperative Institute for Climate, Ocean, & Ecosystem Studies, 3737 Brooklyn

469 Ave. NE, University of Washington, WA 98105 USA, and NOAA-PMEL, 7600 Sand Point Way

470 NE, Seattle, WA 98115 USA

471 Lilian Lucas – Dept. of Geology, University of Illinois at Urbana-Champaign, Urbana, IL 61801

472 USA

473 Aggeliki Georgiopoulou – UCD School of Earth Sciences, University College Dublin, Belfield,

474 Dublin 4, Ireland. Now at: Ternan Energy, Chichester, West Sussex PO19 1UU, UK

475

476 **Corresponding author email:**

477 Uri ten Brink. utenbrink@usgs.gov

478

479

480 **Figures**

481 **Figure 1.** Shaded relief bathymetry of Mona Rift and Mona Passage off western Puerto Rico.

482 Circles – Reported observations sites of tsunami flooding listed in Table 2. Solid red rectangles –
483 Surface projection of the two-segmented normal fault, modeled as the tsunami source (see
484 Discussion). Dash-dotted blue line – Tsunami source fault modeled by Mercado and McCann
485 (1998). Yellow curve – Landslide tsunami source of López-Venegas et al. (2008; 2015). Large
486 and small white star – proposed epicenter of the 1918 earthquake and aftershocks (ISC-GEMS
487 catalog). Black stars – Proposed epicenter of Doser et al. (2005) and isoseismal epicenter of Reid
488 and Taber (1919). Black lines – ROV dive tracks NA035-H1301 and EX-1502-05. Double lines
489 – Seismic lines Pelican Line 62 shown in Figure 7 and EW9605-1298 shown in Figure 8 of
490 Mondziel et al. (2010). Dashed rectangle – Location of inset A. Inset A - Enlargement of the
491 eastern wall of Mona Rift with dive track EX-1502-05. Brown contours – 500 m depth contours.
492 Inset B – Regional location map showing extent of map (dashed rectangle) and location of the
493 Loíza site in Puerto Rico.

494

495 **Figure 2.** Enlargement of the landslide scar at the southern end of Mona Rift. See Figure 1 for

496 location. Black line - dive track NA035-H1301. Arrows point to site of dive images samples

497 shown in Figures 3-6 and locations of push cores 038 and 040 discussed in text. Brown contours

498 –Contours of water depth at 500 m interval.

499

500 **Figure 3.** Image of jagged gouges in the floor of the landslide scar. Downslope direction is into

501 the page. See Figure 2 for location.

502

503 **Figure 4.** (A) grab sample 2013 NA-03-039 from a gully at the scar floor at water depth of 1987
504 m (see Fig. 2 and 5A for location) White spots are scratches caused by the ROV arm extracting
505 the sample. (B) Sample cut in half to reveal the thickness of the Fe-Mn coating and fossiliferous
506 biomicrite interior. (C) Photo of the ROV arm dislodging the sample from the surrounding rock.
507 Only the rock surface exposed to seawater will show Fe-Mn coating. (D) Photo of the ROV arm
508 extracting the push core used for sediment dating.

509

510 **Figure 5.** (A) Image of a gully cutting the floor of the landslide scar. (B) An asymmetric gully
511 within the floor of the landslide scar. Note the white rock ledge at the base of the slope. See
512 Figure 2 for locations of (A) and (B). Other apparent color variations in the rock face are due to
513 variations in distance between the lighting source and the rock face. W.d. – Water depth.

514

515 **Figure 6.** Images of part of (A) the southern and (B) the eastern escarpments of the landslide
516 scar. See Figure 2 for locations of (A) and (B).

517

518 **Figure 7.** Portion of high-resolution multichannel seismic Line 62 crossing the SE wall of Mona
519 Rift, the possible rupture location of the 1918 earthquake and tsunami. See Figure 1 for location.
520 Red lines – interpreted normal fault traces. The line was collected by the USGS aboard the R/V
521 Pelican.

522

523 **Figure 8.** Initial sea surface and sea floor displacement in the tsunami model due to the rupture
524 of a two-segmented normal fault discussed in the text. Contours are simplified bathymetry (in
525 m).

526

527 **Figure 9.** Calculated marigrams at the observation sites listed in Table 1. Observation sites are
528 shown in Figure 1. Missing negative parts of the marigrams at several sites occurs when the
529 seafloor gets exposed (dry) during water withdrawal because calculated sites are located at water
530 depths between 0.5 m and 2 m. Dashed red line - Maximum observed tsunami height from Reid
531 and Taber (1919). Two lines are marked where a range of heights was quoted. Red arrows -
532 Observed arrival time of the tsunami wave, described in Reid and Taber (1919) and listed in
533 “Data and Resources”. The arrow directions describe rising water (up arrow) or receding water
534 (down arrow). Arrows are separated by a horizontal line denote range of arrival time.

535

536 **Figure 10.** Calculated maximum tsunami wave amplitude along the west coast of Puerto Rico
537 due to the two-segmented normal fault along the east wall of Mona Rift. Rectangles – Areas
538 modeled using 10 m grid spacing. White circles – Locations of tsunami observations in Reid and
539 Taber (1919). Insets A and B – Enlargements of the rectangles near Mayagüez and Boquerón.

540

541 **Figure 11.** (A) Slickensides (pointed by white arrows) on plutonic(?) rock. See inset B in Figure
542 1 for location. “White flower” – Sponge (B) massive plutonic(?) rock without Fe-Mn crust.
543 Enlargement - A small blueish smooth surface, possibly, an exposed fault plane in direction
544 280°. The rock may be a blueschist outcrop.

1 **Table 1.** Comparison between Reid and Taber (1919) tsunami observations and model
 2 calculations. See Figure 1 for locations of observation.

	Location of observation	Lat. (Degree Decimal minute)	Long. (Degree Decimal minute)	Obs. Wave height (m)***	Calc. pos- itive amp. (m)	Obs. first wave polarity	Calc. first wave polarity	Reported arrival time (min.) and its polarity ****	Calc. arrival time(min.) matching polarity description
1	Pt. Agujereada	18°30.47	-67°08.24	5.5-6	6.7		N*		
2	Pt. Borinquen lighthouse	18°29.32	-67°09.7	4.5	4.6	N*	N		
3	Aguadilla	18°25.5	-67°09.3	2.4-3.4	2.4		N	5-6 P	6 P
4	Columbus (Colon) Park, Aguadilla	18°24.83	-67°09.73	>4	4		N		
5	Pt. Higüero lighthouse	18°21.82	-67°16.25	5.2	6	N	N		
6	Mayagüez	18°12.33	-67°09.2	1.1-1.2	1		N	25-30 P	25-32 P
7	Boquerón	18°01.56	-67°10.47	1	0.8	N	N	60 N	43-49 N
8	Rio Grande de Loíza	18°26.33	-65°52.61	1	0.7	Slight P*	Slight P*	25-30 N P	25-28 N P
9	Mona Is.**	18°05.28	-67°56.39	>4					

3 * - N-Negative (withdrawal); P – Positive (flooding).

4 ** - The lack of near-shore high-resolution bathymetry precludes the calculation of reliable amplitude.

5 *** - The observations did not specify the tidal condition. Tidal range around Puerto Rico is ≤ 0.5 m

6 (<https://tidesandcurrents.noaa.gov/>).

7 **** - Reported eyewitness arrival time and its described wave polarity. (See text in Data and Resources for detailed
8 description).

9

10 **Table 2. Fault rupture parameters for the tsunami model**

Segment	Length (km)	Downdip width* (km)	Slip (m)	Lat. (deg. Dec. min.)	Long. (deg. Dec. min.)	Lat. (deg. Dec. min.)	Long. (deg. Dec. min.)	Strike (°)	Dip (°)	Rake (°)
1	29	15	4.32	18°51.67	-67°18.14	18°36.18	-67°20.98	190	60	-90
2	11	15	4.32	18°34.09	-67°18.65	18°32.18	-67°13.50	109	60	-90

11 *- Fault top is at 1 km depth.

12 ** - shear modulus, $\mu = 3 \times 10^{10}$ Pa.

Figure 1

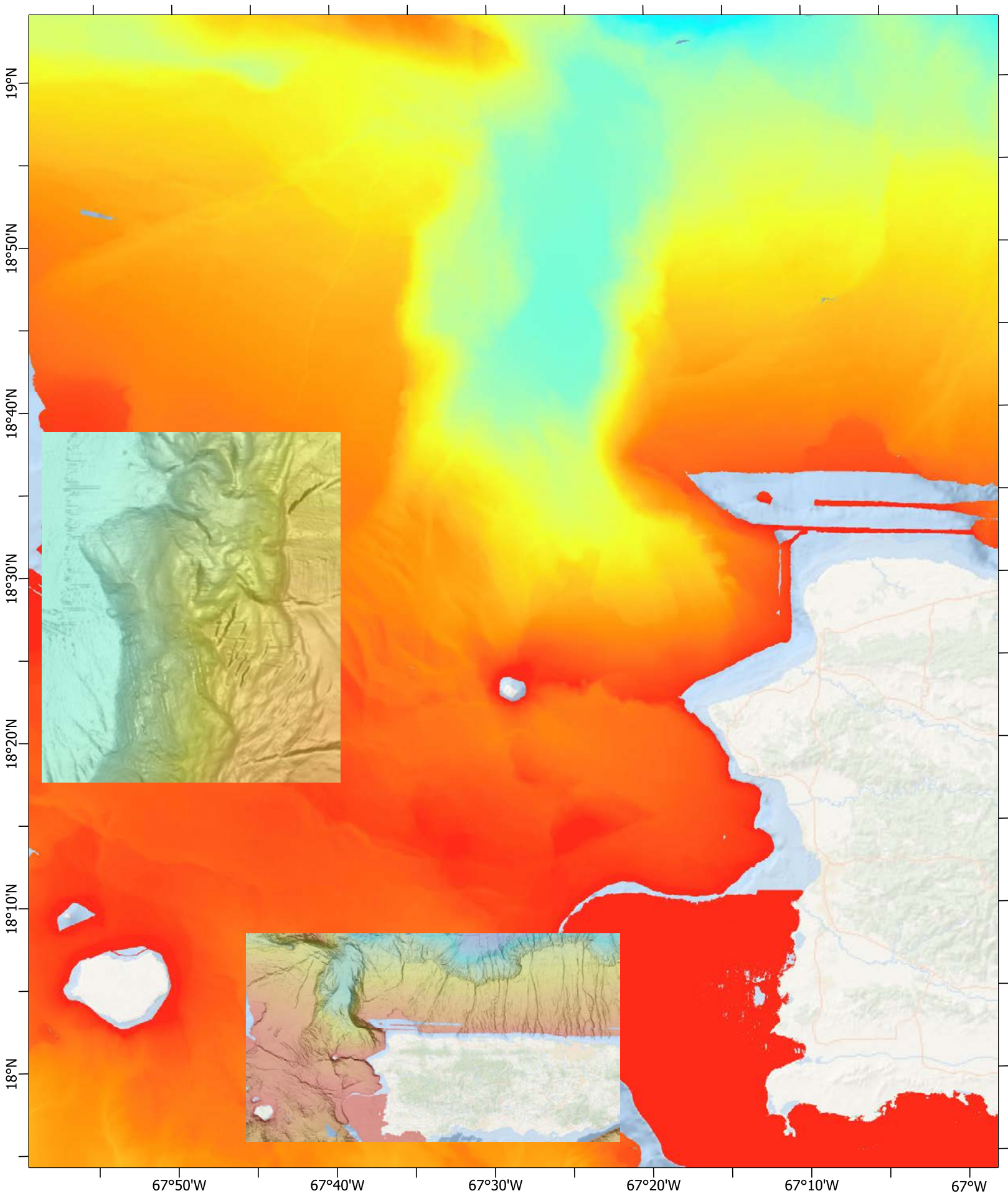


Figure 2

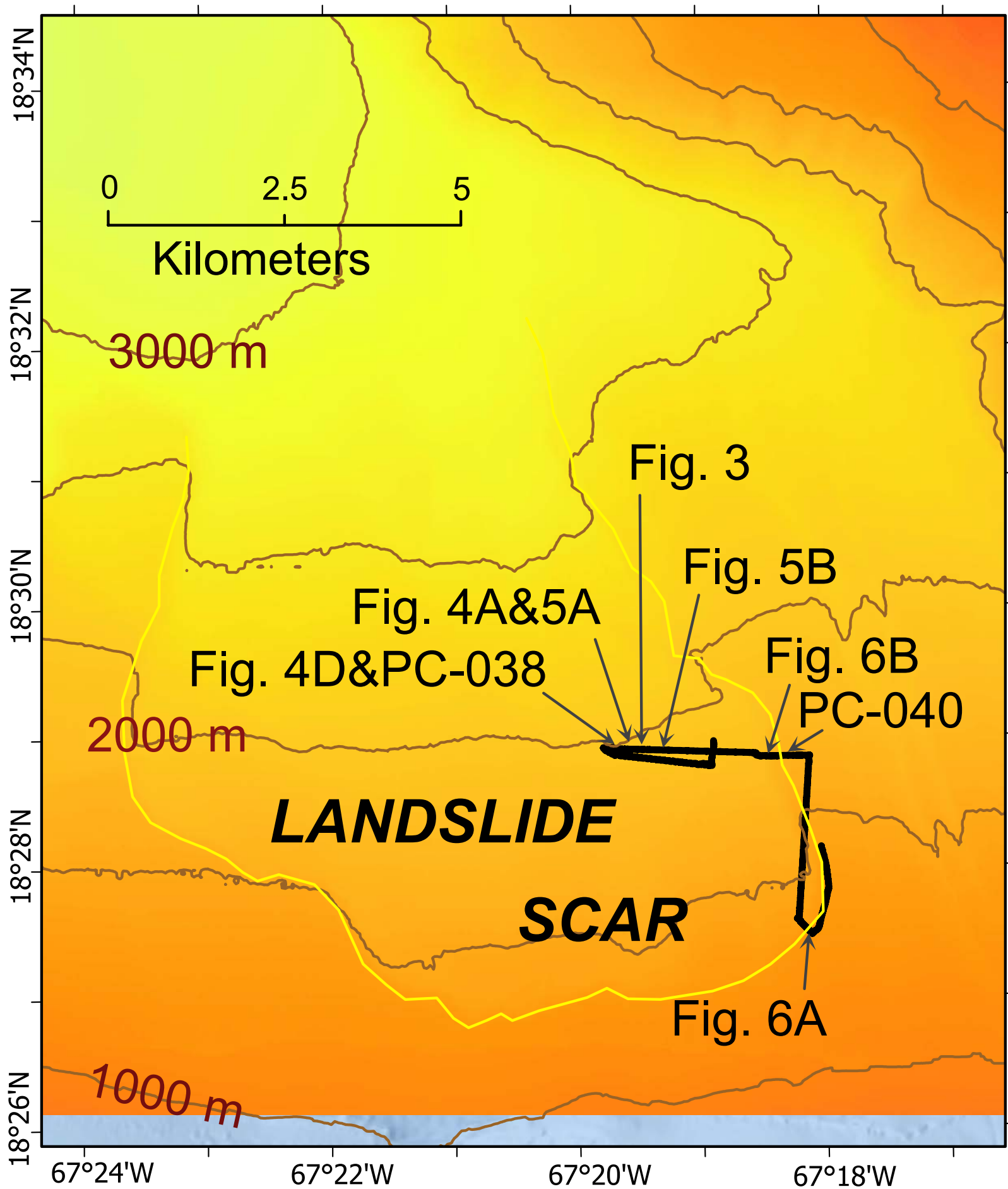


Figure 3

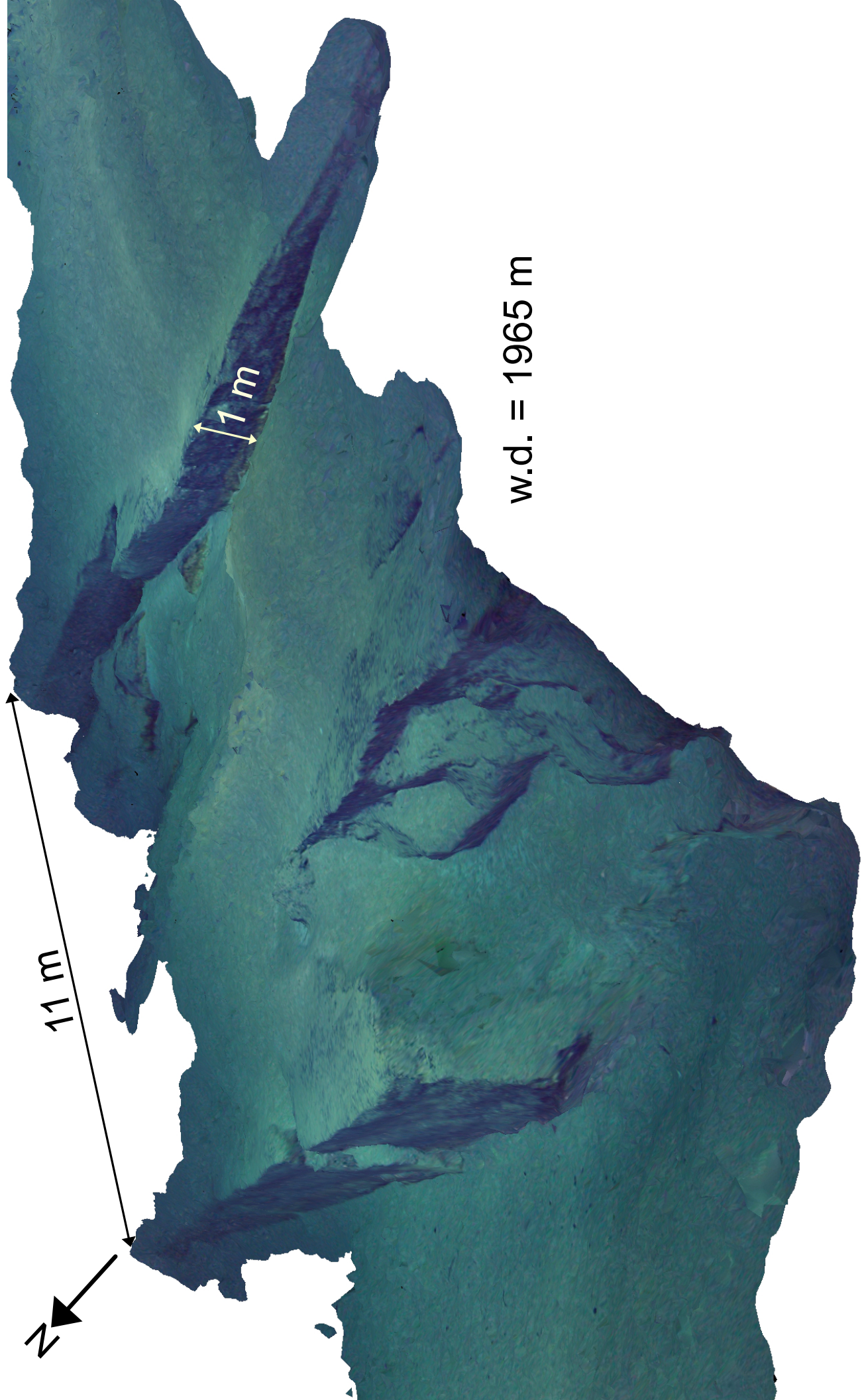


Figure 4

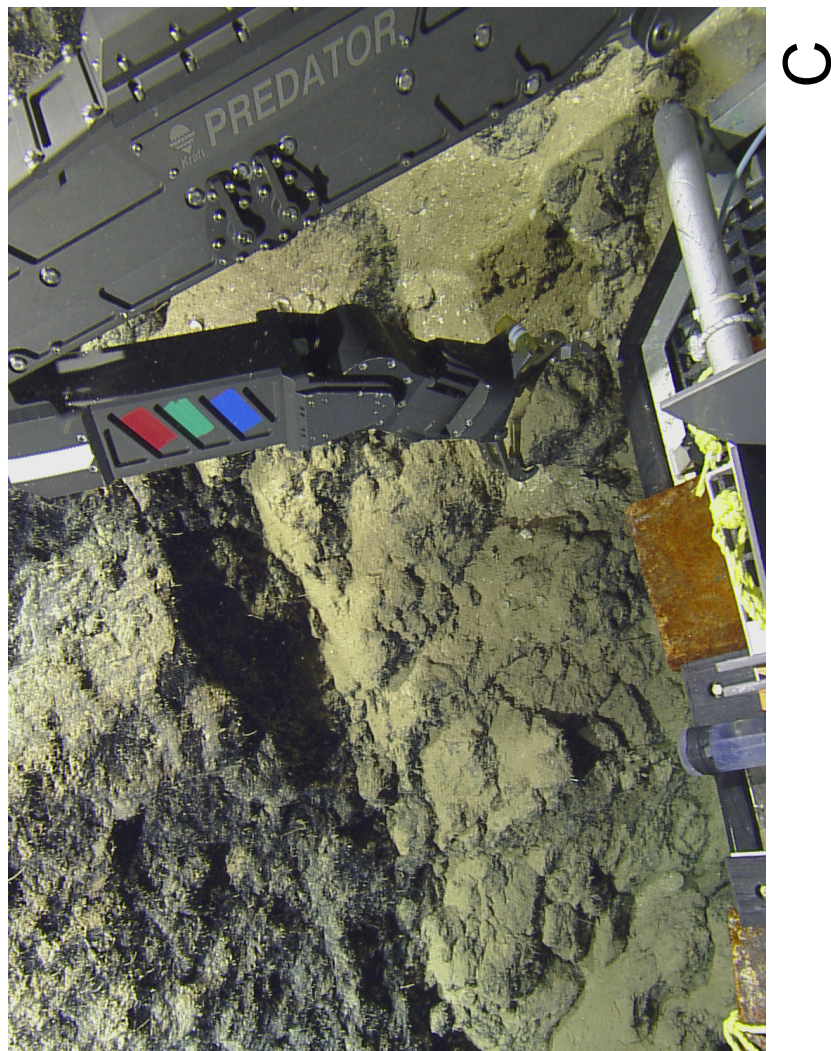
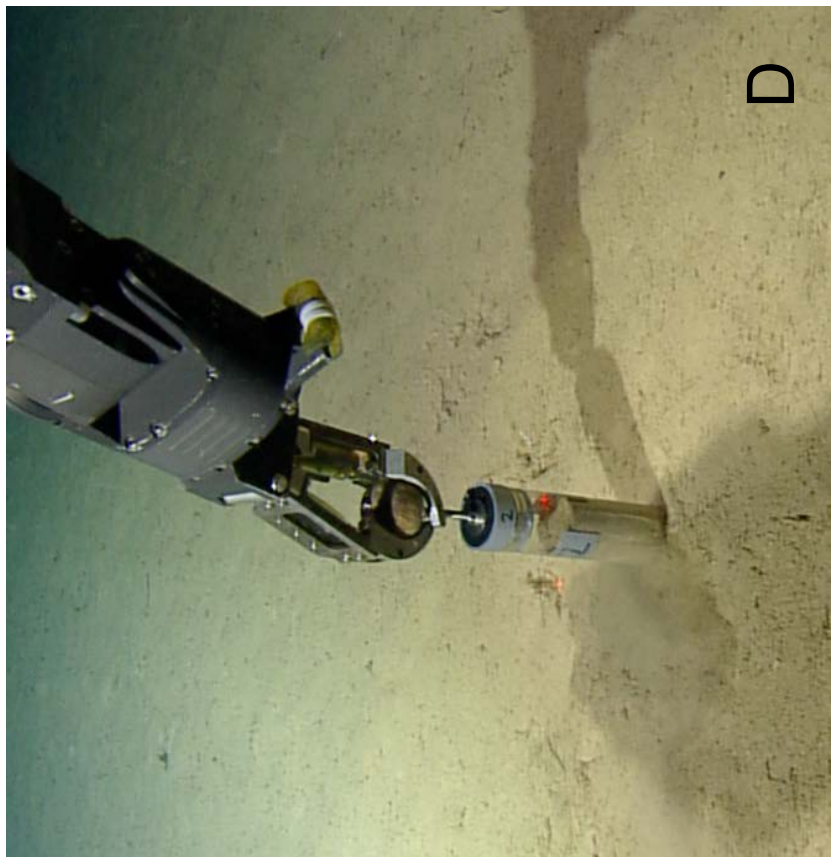


Figure 5

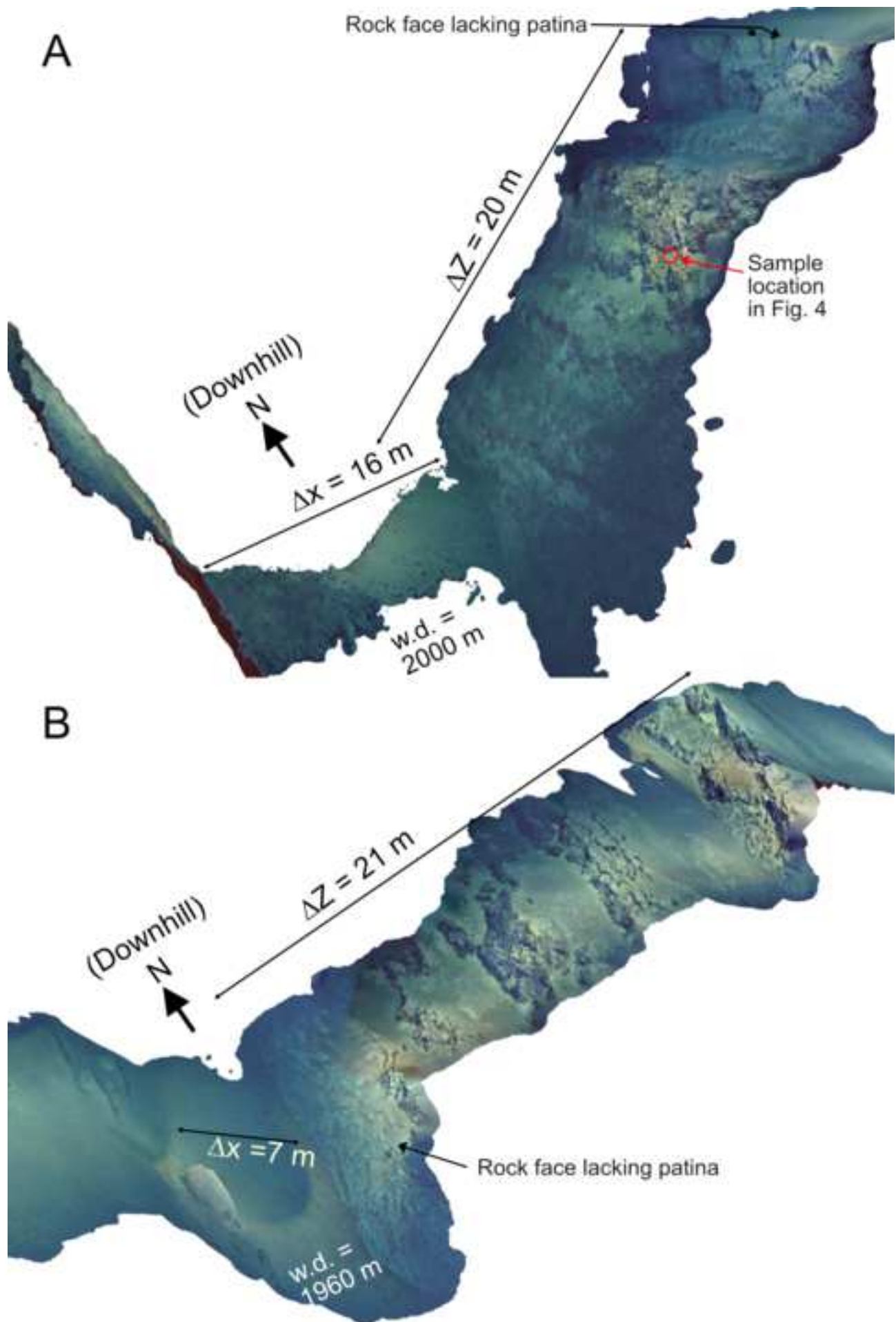


Figure 6

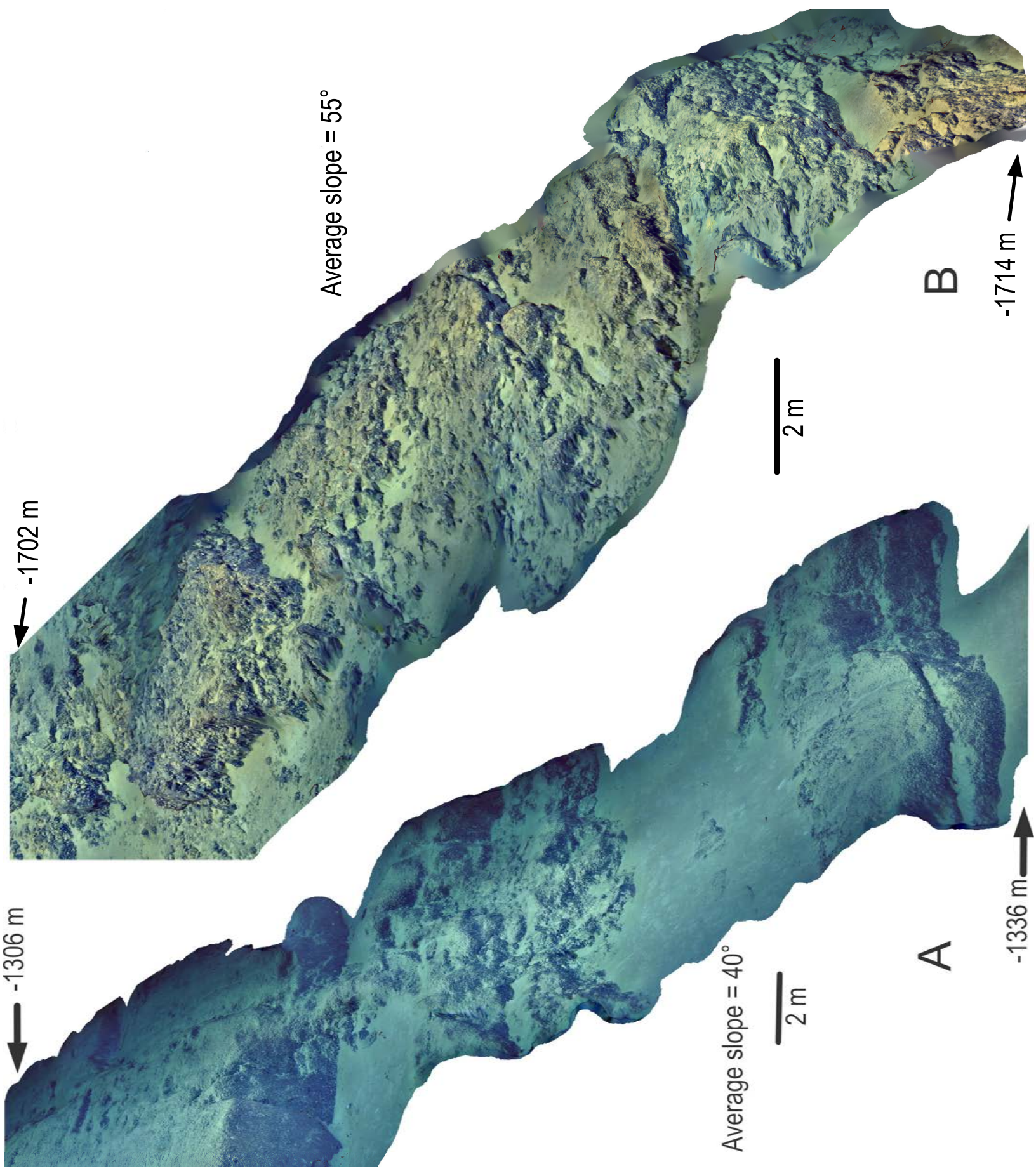


Figure 7

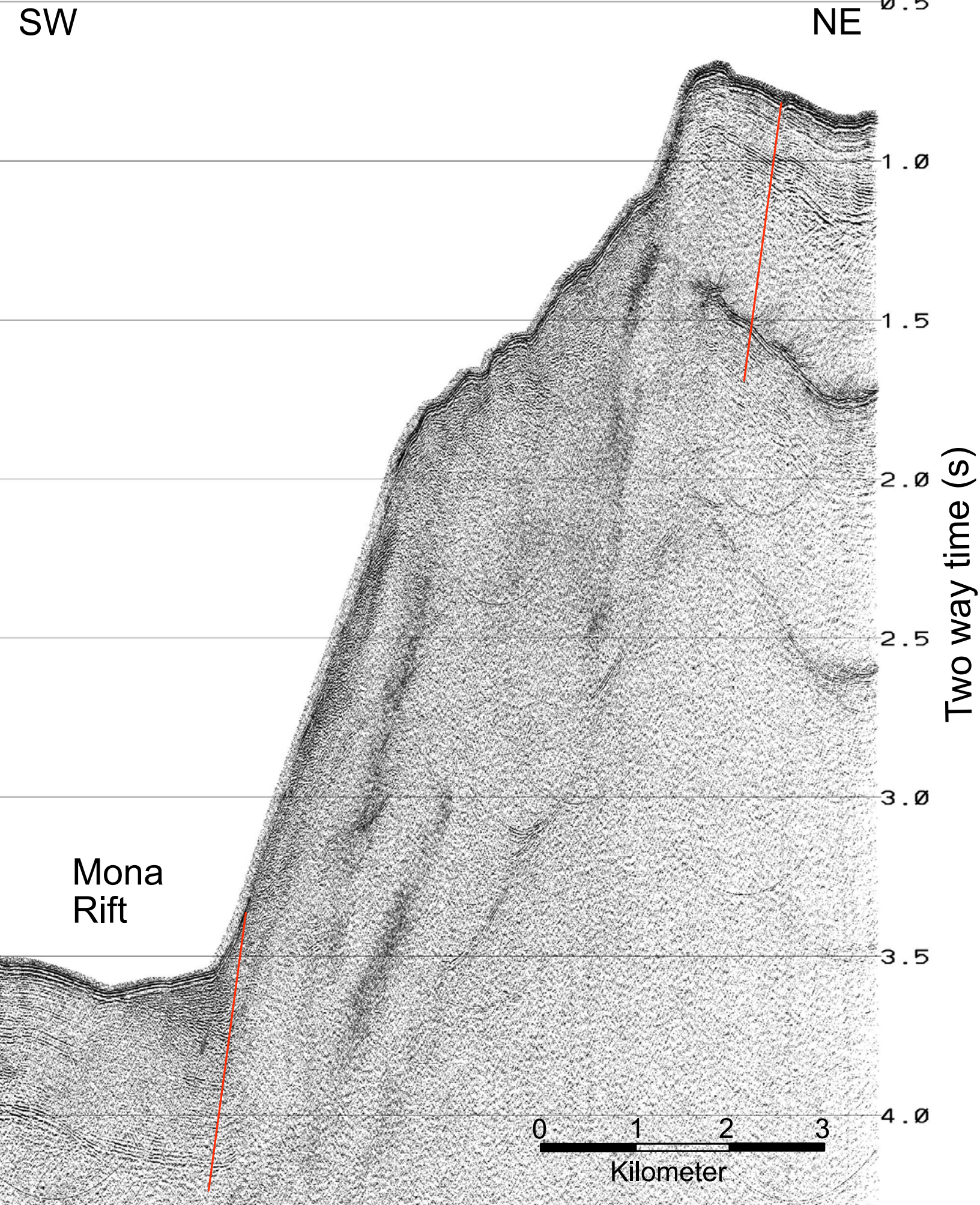


Figure 8

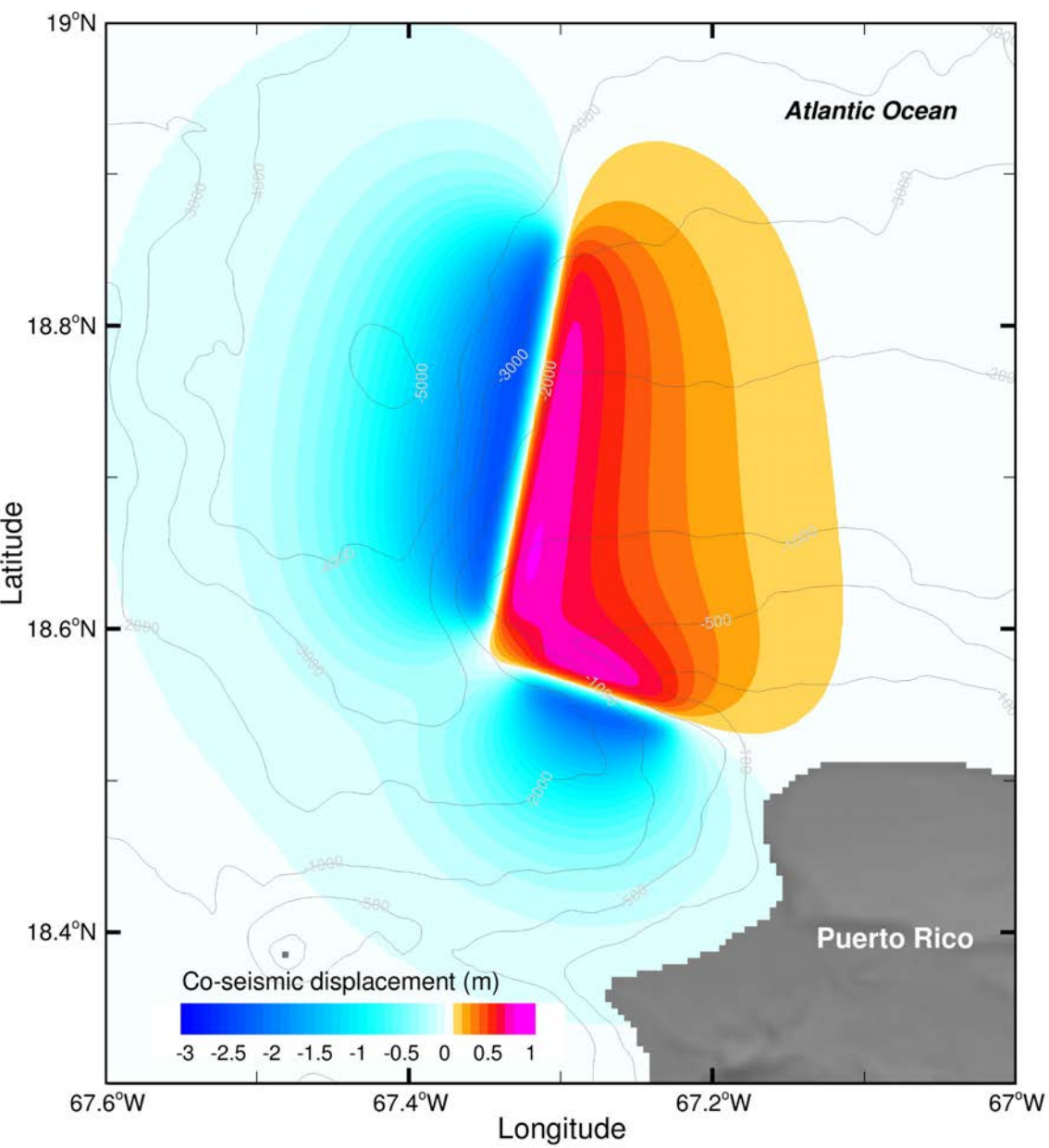


Figure 9

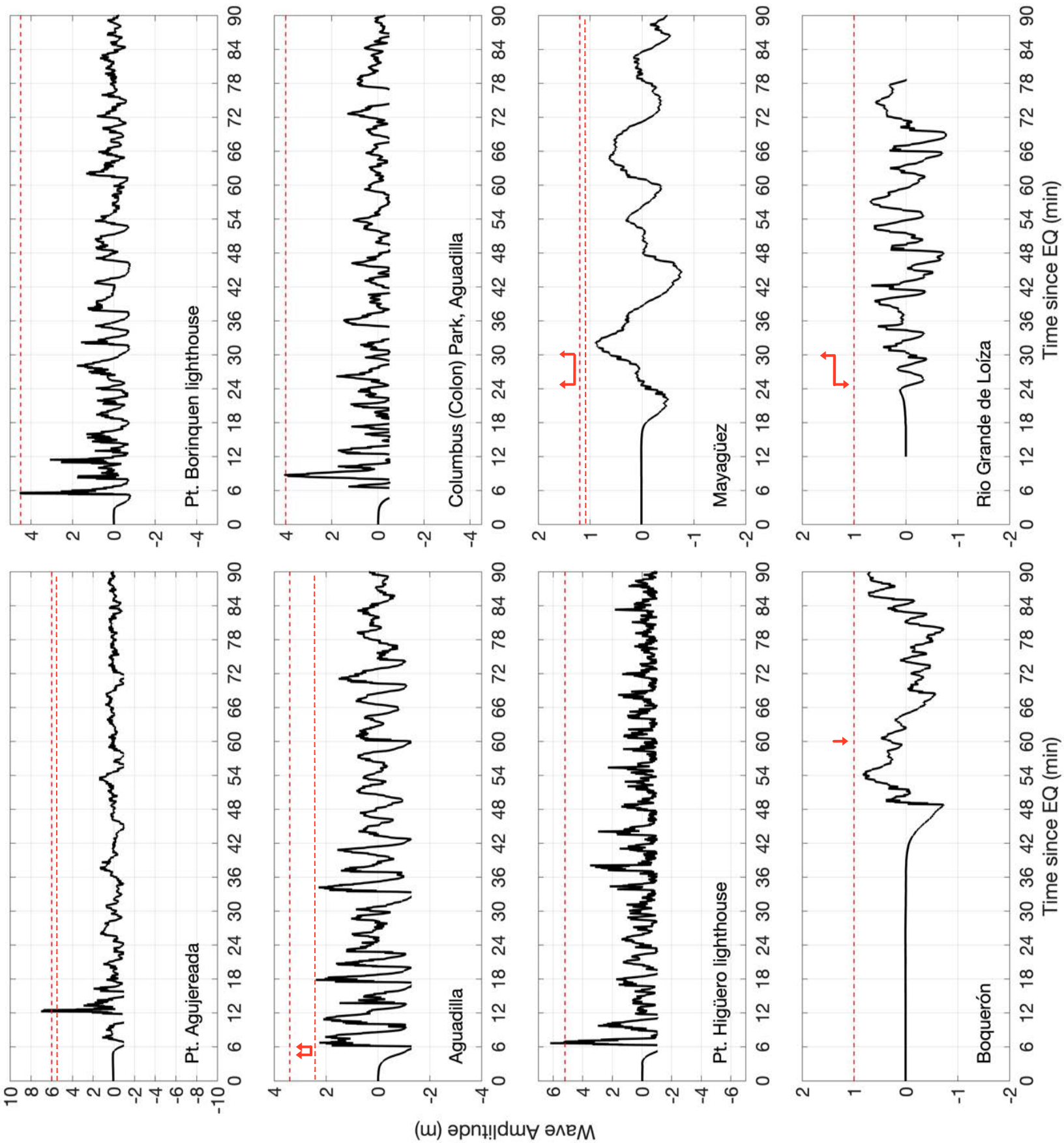


Figure 10

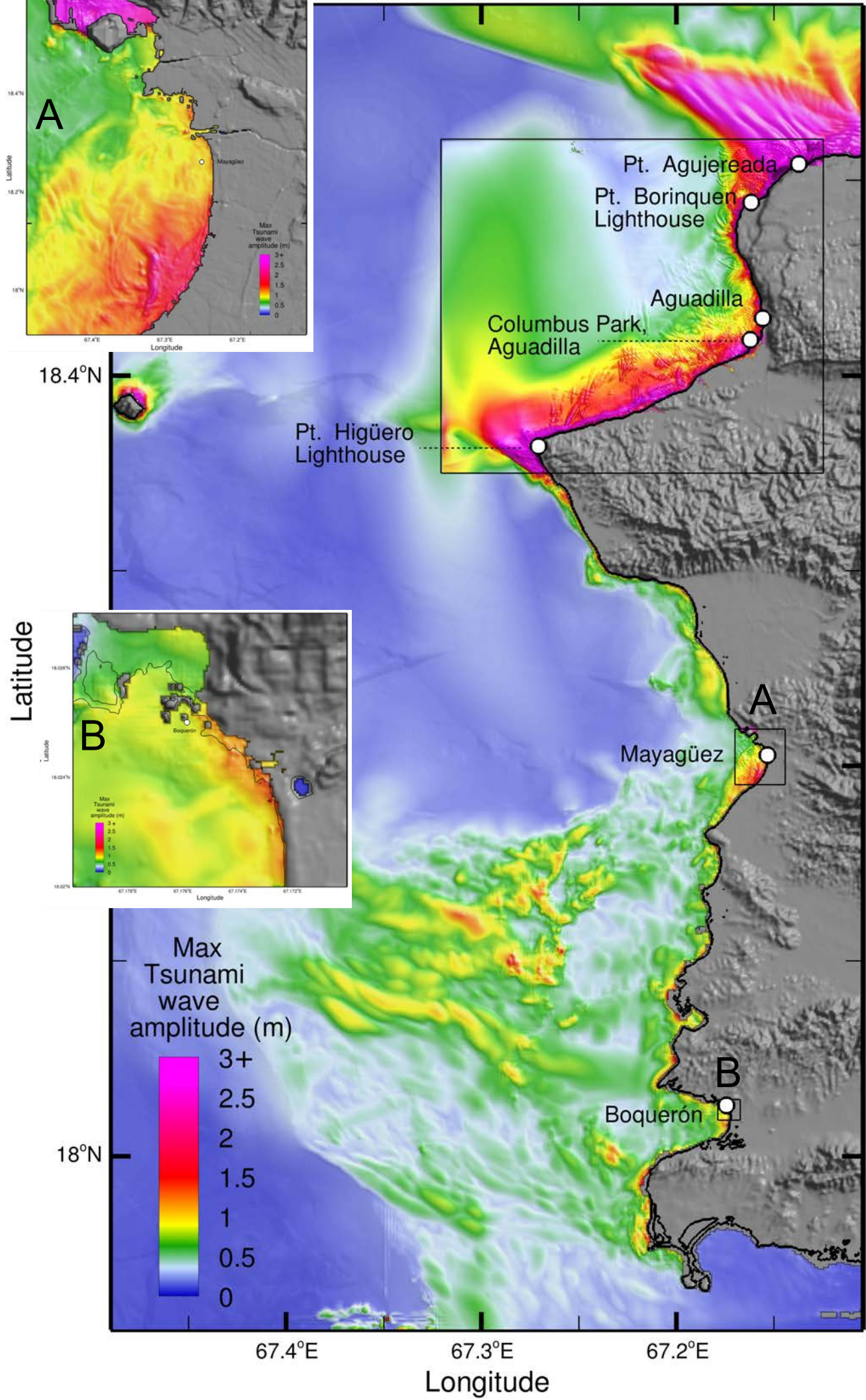


Figure 11

